

Article

Improved Method for Preparing Nanospheres from Pomelo Peel to Achieve High Graphitization at a Low Temperature

Lingdong Zeng¹, Youbin Wang¹ , Yixuan Guo¹, Xiang Dai¹, Liu Chen¹ , Chunlin He¹ ,
Nguyen Thi Hong Nhung¹ , Yuezhou Wei² , Gjergj Dodbiba³  and Toyohisa Fujita^{1,4,*} 

¹ School of Resources, Environment and Materials, Guangxi University, Nanning 530004, China; ldzeng2020@163.com (L.Z.); wangyoubin@gxu.edu.cn (Y.W.); a406510695@163.com (Y.G.); daixiang169@163.com (X.D.); chenliu@st.gxu.edu.cn (L.C.); helink1900@126.com (C.H.); hnhung_2912@yahoo.com (N.T.H.N.)

² School of Nuclear Science and Technology, University of South China, Hengyang 421001, China; yzwei@gxu.edu.cn

³ Graduate School of Engineering, The University of Tokyo, Bunkyo 113-8656, Japan; dodbiba@g.ecc.u-tokyo.ac.jp

⁴ School of Chemistry and Chemical Engineering, Guangxi University, Nanning 530004, China

* Correspondence: fujitayohisa@gxu.edu.cn

Abstract: Biomass waste is a valuable resource that can be recovered, reused, and is renewable. However, converting biomass waste to a high degree of order is a bigger challenge, and graphitization at low temperatures is even more difficult. This paper proposes an improved method (Ni element catalysis) for highly graphitizing pomelo peel at low temperatures (750–900 °C). In this paper, X-ray diffraction (XRD), Raman spectroscopy, X-ray photoelectron spectroscopy (XPS), scanning electron microscopy (SEM), Brunauer–Emmett–Teller (BET), and high-resolution transmission electron microscopy (HRTEM) were used to study the method and the effect of temperature on structural changes during graphitization. Under the improved method, pomelo peel was transformed into nanospherical graphitized material. The degree of graphitization reached 80.23% at 900 °C, which was 31.39% higher than that of the traditional method. Furthermore, through HRTEM, the lattice fringe spacing was observed to be 0.337 nm, which is between pure graphite (0.3354 nm) and amorphous graphite (0.3440 nm). In this paper, the improved method can obtain highly graphitized nanospheres at low temperatures, thus reducing energy consumption, reducing environmental pollution, and promoting sustainable development.

Keywords: pomelo peel; nanospheres; highly graphitized; low temperature



Citation: Zeng, L.; Wang, Y.; Guo, Y.; Dai, X.; Chen, L.; He, C.; Nhung, N.T.H.; Wei, Y.; Dodbiba, G.; Fujita, T. Improved Method for Preparing Nanospheres from Pomelo Peel to Achieve High Graphitization at a Low Temperature. *Crystals* **2022**, *12*, 403. <https://doi.org/10.3390/cryst12030403>

Academic Editor: Jolanta Prywer

Received: 27 February 2022

Accepted: 15 March 2022

Published: 16 March 2022

Publisher's Note: MDPI stays neutral with regard to jurisdictional claims in published maps and institutional affiliations.



Copyright: © 2022 by the authors. Licensee MDPI, Basel, Switzerland. This article is an open access article distributed under the terms and conditions of the Creative Commons Attribution (CC BY) license (<https://creativecommons.org/licenses/by/4.0/>).

1. Introduction

Pomelo is one of the most consumed fruits in the world. The supply and volume of pomelo production in China are the largest in the world [1]. Therefore, the fruit also has a great impact on China's economy. China consumes a lot of pomelos and therefore produces many pomelo peels. Pomelo peels account for about 45% of the total weight and are often treated as agricultural waste [2]. This waste impacts the environment and causes environmental pollution, so it must be properly managed. Because pomelo peel contains cellulose, hemicellulose, and lignin, it is a potential carbon precursor material [3]. Therefore, this paper adopts different methods and temperature regulations to transform pomelo peels into more valuable materials, such as highly ordered and conductive graphitized materials.

Graphitic carbon materials, having attractive physicochemical properties (high electrical conductivity, thermal conductivity, and a high melting point), can be used for many applications, such as supercapacitors, fuel cells, and lithium-ion batteries [4–6], and more and more people are paying attention. The general methods for graphitization include arc

discharge method, laser vaporization [7], and plasma and thermal chemical vapor deposition [8]. However, these methods tend to be complex and require very high temperatures (>2000–3000 °C) [9,10]. Due to various limitations, these methods cannot be widely used, so it is necessary to simplify the method and lower the temperature of graphitization methods. In addition, some studies that use non-renewable resources for graphitization, such as asphalt [11] and coal [12], also raise concerns about sustainable development. Therefore, there is a need to develop renewable resources. On the other hand, biomass materials are considered sustainable materials, and they are a good carbon precursor due to their easy availability and low price [13,14]. At present, catalytic graphitization is a method that can reduce energy consumption and graphitize biomass. This method can use transition metal salts (Fe, Ni, Co, Mn, etc.) as catalysts [15–20] to convert amorphous biomass into highly ordered graphitic nanomaterials using pyrolysis [9,18]. For example, Fredina Destyorini et al. used $\text{NiCl}_2 \cdot 6\text{H}_2\text{O}$ to catalyze coconut peel at 1200 °C to obtain a graphitized carbon material with an IG/ID ratio of 1.16 [21].

This paper adopts different synthesis paths to lower the temperature of synthesizing graphitized carbon materials and convert waste pomelo peels into highly graphitized materials. In this paper, by comparing the synthesis effect of the traditional method and the improved method, it was found that after the improvement of the method, a high degree of graphitization effect could be achieved at a lower temperature. With the improved method, the graphitization effect at 750 °C was better than that at 900 °C with the traditional method. In exploring the temperature, it was found that after the improved method, graphitic carbon nanomaterials were formed under treatment at 900 °C, which was significantly lower than that of the conventional method.

2. Materials and Methods

2.1. Material

The pomelo peels in this work were sourced from the vegetable market in Nanning City, Guangxi Province. Hydrochloric acid (HCl, concentration 37%), sulfuric acid (H_2SO_4 , purity 98%), and anhydrous ethanol ($\text{C}_2\text{H}_6\text{O}$, purity 99.5%) were procured from Guangdong Guanghua Technology Co., Ltd., Shenzhen, China. Potassium permanganate (KMnO_4 , purity $\geq 99.5\%$) and nickel nitrate ($\text{Ni}(\text{NO}_3)_2 \cdot 6\text{H}_2\text{O}$, purity $\geq 99\%$) were sourced from Tianjin Aopusheng Chemical Co., Ltd, China. Deionized water was provided by Shanghai Hetai Ultrapure Water System, Shanghai, China. All reagents were analytical grade.

2.2. Method

Wasted pomelo peels were treated with two methods (Figure 1). The collected pomelo peels were first washed with tap water and then washed with deionized water. Next, they were dried in an oven at 80 °C for 24 h, crushed by a crusher, and powders smaller than 147 μm in size were selected to obtain a relatively uniform fine powder.

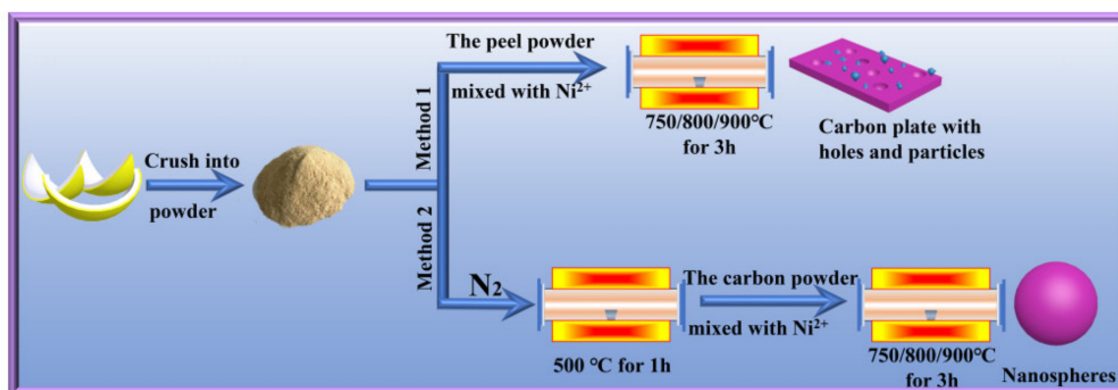


Figure 1. Schematic flow diagram of the traditional method and the improved method.

The first method used impregnated pomelo peel powder in a mixture of nickel nitrate and 100 mL absolute ethanol (5 mM metal/g powder). This was then dried in an oven at 70 °C for 8 h and heated to (750 °C/800 °C/900 °C, 3 °C/min) in a tube furnace with N₂ atmosphere. Then, the obtained carbon powder was washed with 20% hydrochloric acid and then condensed and refluxed for 2 h with a mixed solution of H₂O/H₂SO₄/KMnO₄ = 1:0.02:0.006 (molar ratio) to purify the biochar. Next, the biochar was washed with 10% hydrochloric acid to remove MnO₂ and then washed several times with deionized water. The second method was to heat the powder to 500 °C (5 °C/min, 1 h) in a tube furnace under N₂ atmosphere to obtain carbonized powder. The remaining steps were the same as method one.

The following nomenclature T-M was used, where T stands for temperature and M stands for method (see Supplementary Materials Table S1).

2.3. Characterization of the Peel Biomass

The X-ray powder diffraction (XRD) analysis of the samples was conducted on the Bruker D8 instrument. The operating condition was 40 kV and 30 mA, using Cu K α radiation ($\lambda = 0.15406$ nm) over the scan angle (2θ) range of 10°–80° (2°/min). X-ray photoelectron spectroscopy (XPS) analyzed the surface chemistry and chemical state of sample elements. XPS was performed on Thermo Scientific. XPS parameters included analytical capabilities (wide: 75 W, narrow: 150 W) and monochromatic Al K α . The data acquisition time was 2 min 16 s. The XPS peaks were fitted by deconvolution using Avantage software. Raman spectra were taken in a Raman microscope (Via Reflex) with a laser excitation wavelength of 532 nm to analyze the degree of order of carbon structure. The scanning range was 500–3500 cm^{−1}, and the data-acquisition time was 10 s. Each sample was tested at three different points to ensure data accuracy. Analysis of Raman spectra was performed by peak deconvolution using Peakfit software. Fourier transform infrared (FTIR) spectroscopy was performed using a spectrometer (Nicolet iS 50) to investigate the changes of functional groups during graphitization. The scanning range of FTIR was 800–4000 cm^{−1}. Curve processing was performed by Origin software. Before measurement, samples were degassed in vacuum at 200 °C for 6 h, as determined by nitrogen adsorption–desorption method using Brunauer–Emmett–Teller (BET) theory to determine the specific surface area and pore structure. HRTEM was used to observe lattice fringes. HRTEM was performed on (FEI Talos F200S). All samples for HRTEM analysis were dispersed in ethanol and sonicated for 10 min to ensure uniform dispersion. They were dropped on carbon-coated grids followed by drying process at room temperature. This was used to detect images and lattice fringes of a sample. SAED was used to confirm the degree of graphitization and was performed on FEI Talos F200S.

3. Results and Discussions

The degree of graphitization of the samples was analyzed by the XRD spectrum. The order degree of carbon structure was analyzed by Raman spectroscopy. It can be seen from Figure 2a that there are apparent sharp peaks at (ca. 26°, 43°, 54°, 78°, 83°), for the corresponding (002), (100), (101), (004), and (110) diffraction peaks (PDF#41-1487). This shows that the waste pomelo peel has good graphitization with the catalysis of the Ni element. In Figure 2a, it can be seen that the (002) diffraction peaks of 750-1, 800-1, and 900-1 show increasingly sharper degrees as the temperature increases. The pomelo peel carbonized at 500 °C showed a broad hump at $2\theta = 23^\circ$ and 44° , indicating that it was in an amorphous state (Figure S1) [21]. We can see that the (002) diffraction peak of the 750-2 sample is sharper than that of the 900-1. The 750-2 and 800-2 samples are similar in sharpness, and the 900-2 sample appears sharper. The following are the criteria for evaluating the degree of graphitization [22–24]:

$$D(002)(\text{\AA}) = \lambda / 2\sin\theta_{002} \quad (1)$$

$$G = (0.3440 - d_{002}) / (0.3440 - 0.3354) \quad (2)$$

where λ is the wavelength of the X-ray radiation and θ_{002} is the (002) reflection angle; 0.3354 nm is the interlayer spacing of graphite, and 0.3440 nm is the value of carbon without graphite order.

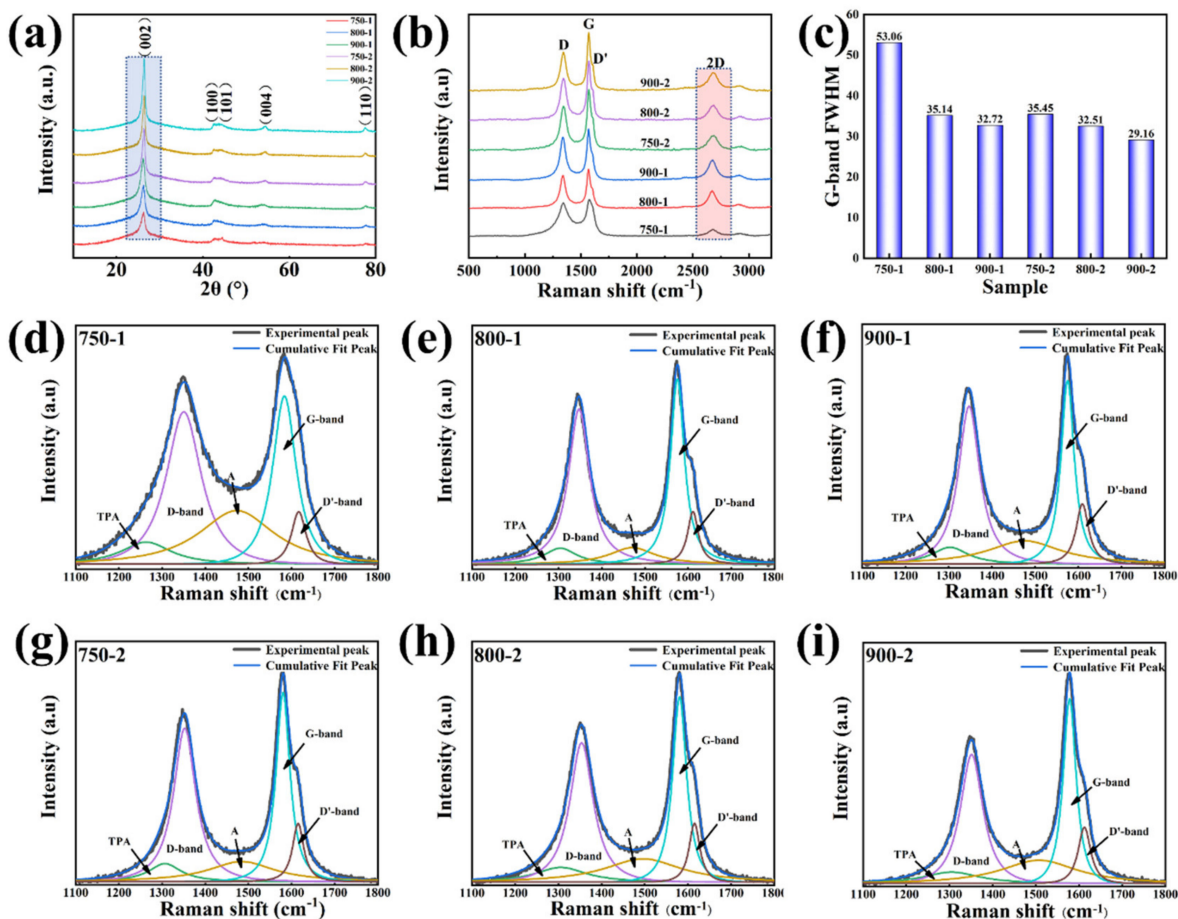


Figure 2. (a) XRD patterns of the graphitized pomelo peel; (b) Raman of the graphitized pomelo peel; (c) FWHM of G-band; Deconvolution of Raman spectra for (d) 750-1, (e) 800-1, (f) 900-1, (g) 750-2, (h) 800-2, (i) 900-2.

According to the XRD spectrum (Figure 2a), the structural parameters of graphitic carbon were calculated. Therefore, the plane spacing $d(002)$ was calculated by the Bragg equation to calculate the diffraction peak of (002) (Table 1). The interlayer spacing $d(002)$ of 750-1, 800-1, and 900-1 is significantly larger than that of graphite (0.3354 nm), indicating that the samples have turbo stacking [25]. The samples synthesized by method two are highly ordered. The graphitization degree of 750-2, 800-2, and 900-2 is 74.42–80.23%, of which the 900-2 sample has a high degree of graphitization (80.23%), which is slightly lower than that of commercial graphite (90.23%) [26]. The degree of graphitization of 750-1, 800-1, and 900-1 is 19.77–48.84%, and the degree of graphitization of 900-2 is higher than that of 900-1 (31.39%), indicating that method two is more conducive to catalyzing waste pomelo peel graphitization.

Figure 2b is the graph of Raman spectroscopy, which is used to study the degree of order of the samples. In the first-order Raman spectrum (1200–1700 cm^{-1}), there are two strong peaks at ca. 1339 and 1568 cm^{-1} corresponding to the D-band and G-band, respectively. At the shoulder of the G band, there is a shoulder at about 1610 cm^{-1} , called the D' band [25,27]. The D band represents the disordered graphitic structure and is associated with defects in the graphitic sp^2 carbon structure [28,29]. The G-band is related to the vibrational mode of E_{2g_2} of sp^2 -bonded carbon atoms, reflecting the graphitic phase in carbon [30–32]. Therefore, the intensity ratio of the G-band relative to the D-band is

widely used to judge the order degree of carbon structure, which is often associated with an improvement in the degree of graphitization [12,33]. The full width at half maximum (FWHM) of the G-band indicates in-plane defects and lateral dimensions [34]. As shown in Figure 2d–i, the Raman spectra of samples in the range of 1100–1800 cm^{-1} were made using a Gauss–Lorentzian curve fitting program. The results of the FWHM analysis of the peak-fitted G-band are shown in Figure 2c. As shown in Figure 2d–i, the Raman spectrum of the samples is deconvoluted into five components: the TPA band related to the trans-polyacetylene-like structure, which is responsible for the shoulder on the left of the D band, the D band; the A-band, which is around 1490 cm^{-1} and assigned to the amorphous structure; the G-band; and the D'-band, which is characteristic of defects caused by the intra-valley double resonance scattering process [28]. As shown in Figure 2c, the FWHM of the G-band decreases gradually with the increase in temperature. In method one, the FWHM of 750-1, 800-1, and 900-1 were 53.06, 35.14, and 32.72, respectively. In method two, the FWHM of 750-2, 800-2, and 900-2 were 35.45, 32.51, and 29.16, respectively. It can be seen that the FWHM of the G-band of the samples prepared by method two is lower, indicating an improved crystal structure as the defects disappear, thereby producing an in-plane homogenization process of ordered graphite. A larger value of IG/ID represents a higher degree of order. In Table 1, it can be seen that the IG/ID values of the 750-1, 800-1, and 900-1 samples are 1.10, 1.17 and 1.19, respectively, indicating the degree of order of the carbon structure increases gradually with the increase in temperature. The IG/ID values of 750-2, 800-2, and 900-2 samples are 1.33, 1.37, and 1.43, respectively, which also reflected the same rule. The value of $\text{ID}/(\text{ID} + \text{IG} + \text{ID}')$ reflects the degree of disorder, and as the ratio decreases, the degree of order increases. The $\text{ID}/(\text{ID} + \text{IG} + \text{ID}')$ values of the 750-1, 800-1, and 900-1 samples are 0.701, 0.655, and 0.641, respectively, which shows that as the temperature increases, the disorder decreases and the order increases. The $\text{ID}/(\text{ID} + \text{IG} + \text{ID}')$ values of the 750-2, 800-2, and 900-2 samples are 0.618, 0.591, and 0.509, respectively, indicating the same rule. A distinct peak appears at about 2690 cm^{-1} corresponding to the 2D band, which is caused by the vibration of the two-phonon lattice, indicating the typical characteristic peak of graphite [35]. From the comparison of the two methods, it is obvious that the degree of order that method two can achieve is higher than that of method one. At the same time, it is proved that method two is more favorable for catalyzing the graphitization of waste pomelo peel. The degree of order trend of Raman is consistent with the XRD analysis results, so it shows that the graphitization effect of method two is better than that of method one.

Table 1. Structural parameters were analyzed from the curve of the XRD and Raman spectrum.

Sample	d_{002} (nm)	G (%)	IG/ID	$\text{ID}/(\text{ID} + \text{IG} + \text{ID}')$
750-1	0.3423	19.77	1.10	0.701
800-1	0.341	34.88	1.17	0.655
900-1	0.3398	48.84	1.19	0.641
750-2	0.3376	74.42	1.33	0.618
800-2	0.3375	75.58	1.37	0.591
900-2	0.3371	80.23	1.43	0.509

FTIR spectral analysis reflects the functional groups of the sample (Figure 3a). The FTIR spectrum shows that the characteristic vibrational peak of O-H is at about 3457 cm^{-1} [36,37]. At about 1635 cm^{-1} , the characteristic vibrational peak of C=C appeared; the characteristic vibrational peak of C-H appeared at about 1395 cm^{-1} ; the characteristic vibrational peak of C-N appeared at about 1123 cm^{-1} [38]. Under different treatment methods and different temperatures, the functional groups of the samples did not change, indicating that other treatment methods did not affect the functional groups of the samples.

The specific surface area and pore structure of pomelo peel samples were tested by N_2 adsorption–desorption experiments. As shown in Figure 3b, the isotherms of the samples belong to the typical integral of the IV isotherms. The sample exhibits an H4-type

hysteresis loop at a moderate relative pressure ($0.4 < P/P_0 < 0.9$), indicating the existence of micropores and mesopores in the samples [27]. The volume and area of the micropores are shown in Table S2. The samples showed an upward trend at high relative pressures ($P/P_0 > 0.9$), indicating macropores due to the accumulation of carbon particles. The pore size distribution is shown in Figure 3c, and the existence of micropores, mesopores, and macropores in the sample is consistent with the results in Figure 3b. The samples 750-1, 800-1, 900-1, 750-2, 800-2, and 900-2 are rich in micropores (pore size < 2 nm), and also have more distribution in the mesoporous part ($2 \text{ nm} < \text{pore size} < 50 \text{ nm}$), but 750-1, 800-2, and 900-2 are less distributed in the macro-porous part [39].

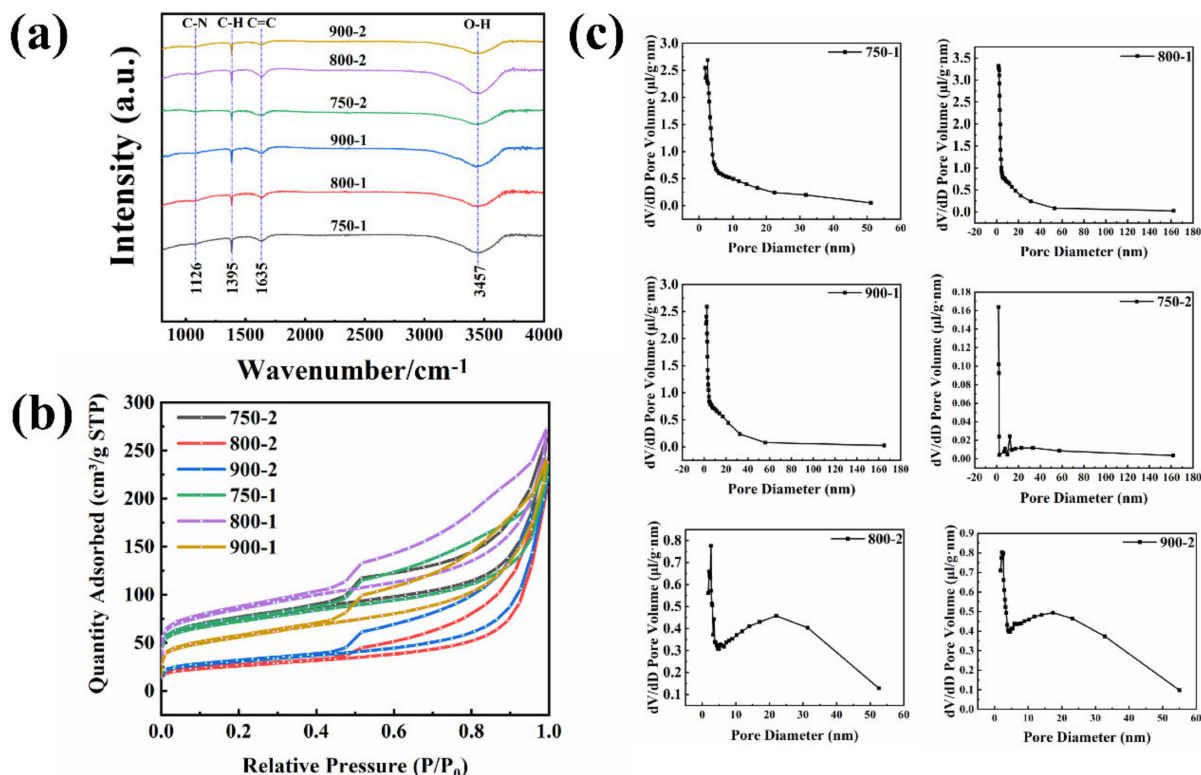


Figure 3. (a) FTIR of the graphitized peel; (b) N_2 adsorption–desorption isotherms for the graphitized peel; (c) Pore size distribution image of the graphitized peel.

To further investigate the morphology of the samples under different conditions, SEM characterization was performed. Under the different processing methods of method one and method two, there are great changes in morphology. Under the treatment of method one, the morphologies of 750-1, 800-1, and 900-1 showed a more and more obvious etching effect of Ni with the increase in temperature and appeared in the state of small particles (Figure S2). After the treatment of method two, 750-2, 800-2, and 900-2 appeared spheroidized (Figure 4a–c). In order to further observe the morphology of pomelo peel under the treatment of method two, high-magnification characterization was carried out (Figure 4d–f). With the increase in temperature, the phenomenon of spheroidization became more and more obvious, the diameter of nanospheres became smaller and smaller, and the number of particles became more and more. As shown in Figure 4g–i, with the increase in temperature, the diameter of the nanospheres gradually decreases, and the average diameters of 750-2, 800-2, and 900-2 are 213.23 nm, 205.32 nm, and 176.8 nm, respectively.

The 900-2 sample showed nanospheres covering the surface of the sample. The difference between the two processing methods brings about the display of two different morphologies. The generation of the two different morphologies may be attributed to the different carbon content. In the carbonized sample, the sample contains a larger proportion

of carbon, and the carbon in the sample has more opportunities to contact Ni, so the degree of graphitization is higher [25,40].

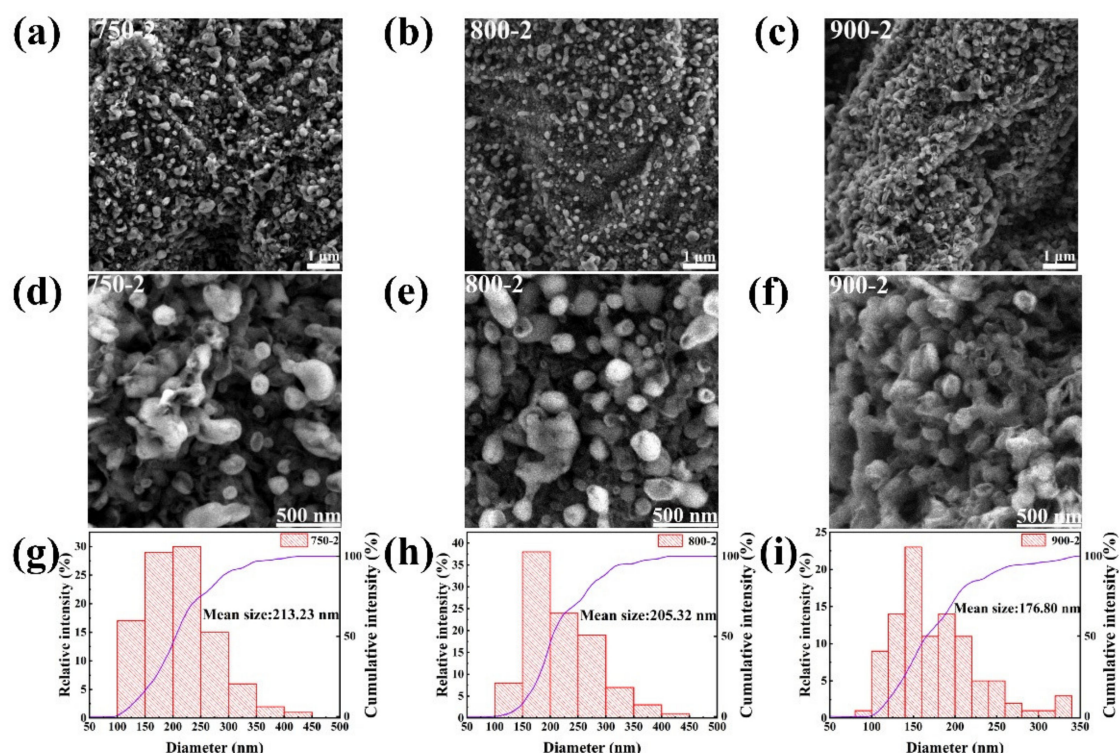


Figure 4. (a,d) SEM images of 750-2; (b,e) SEM images of 800-2; (c,f) SEM images of 900-2; (g–i) Particle size distribution of 750-2, 800-2, 900-2.

XPS spectroscopic characterization was performed to analyze the surface chemical composition of the samples. As shown in Figure S3, the XPS spectra of the samples with binding energies between 0 and 900 eV showed that only three elements, C, N, and O, were present [41]. The XPS spectrum of C1s was further analyzed, and the C1s spectrum was deconvoluted into three peaks. The 284.2 eV can be attributed to the sp^2 -hybridized carbon in the aromatic C=C bond; 284.8 eV and 287.3 eV can be attributed to the amorphous sp^3 -bonded carbon (C-C) and C=O, respectively [26]. For quantitative analysis of carbon atoms to study the degree of graphitization, it is generally necessary to calculate the ratio of sp^2 to sp^3 in the sample [26,42]. As shown in Figure 5a–c, the sp^2 to sp^3 ratios of samples 750-1, 800-1, and 900-1 are 0.99, 1.06, and 1.09, respectively; Figure 5d,e shows that the sp^2 to sp^3 ratios of samples 750-2, 800-2, and 900-2 were 1.17, 1.39, and 1.51. It can be seen that regardless of whether method one or method two is used, the degree of graphitization is closely related to temperature. Between 750 °C and 900 °C, the degree of graphitization increases with the increase in temperature, and the degree of graphitization of method two is much higher than that of method one. The conclusions drawn from XPS on the degree of graphitization are consistent with those from XRD and Raman spectroscopy.

In order to further study method two, the structure and graphitization of 750-2, 800-2, and 900-2 samples were further analyzed by TEM combined with selected area electron diffraction (SAED) (Figure 6). The clear diffraction rings of SAED can be seen from Figure 6a–c, which are (002), (100), (101), (004), (110), and (112) lattice fringes, respectively. Diffraction spots and rings appearing in the SAED image prove that crystalline or graphitic nanostructures formed in the sample. Furthermore, the SAED pictures prove that the degree of graphitization is already high [5,9]. Figure 6d,e shows the HRTEM images of 750-2, 800-2, and 900-2. It can be seen from the figure that the lattice fringes become more apparent as the temperature increases. The spacings between the (002) planes are 0.3376 nm, 0.3375 nm, and 0.3371 nm, respectively, and with the temperature rise, the spacing between

the (002) planes becomes closer and closer to the commercial graphite (0.3362 nm) [26]. TEM and SAED demonstrate the high degree of graphitization of the 900-2 sample, which is consistent with the results of XRD, Raman, and XPS analysis.

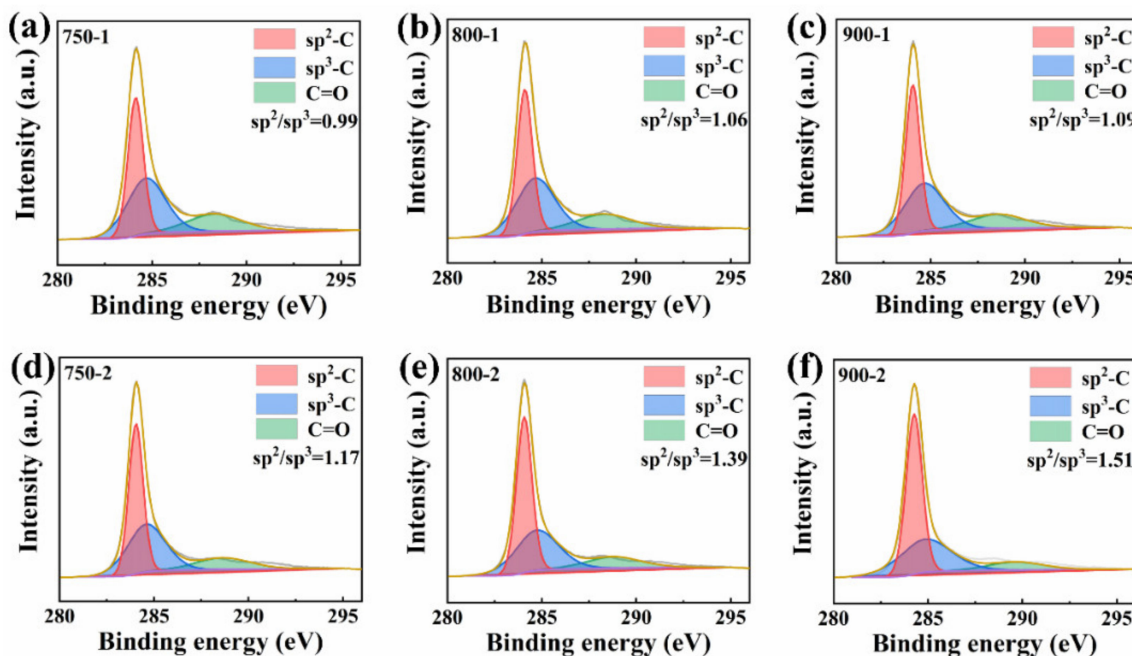


Figure 5. (a) XPS spectrum of C1s for 750-1; (b) XPS spectrum of C1s for 800-1; (c) C1s spectrum for 900-1; (d) C1s for 750-2; (e) XPS spectrum of C1s for 800-2; (f) XPS spectrum of C1s for 900-2.

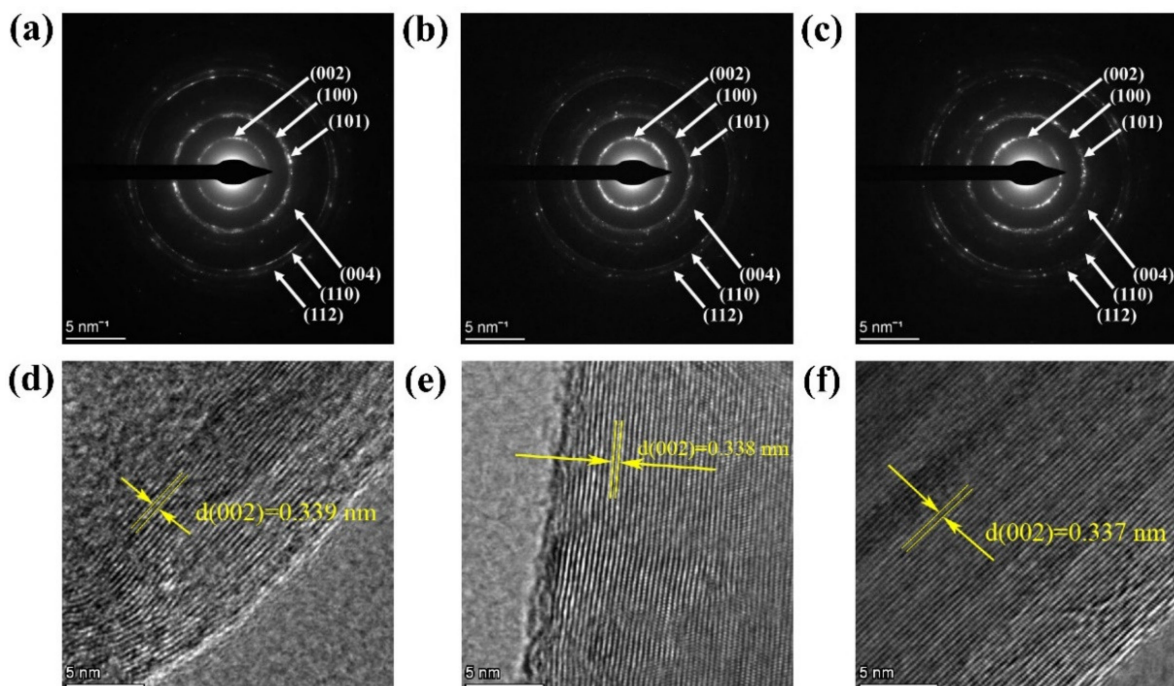


Figure 6. (a–c) SAED pattern of 750-2, 800-2, 900-2; (d–f) HRTEM images of 750-2, 800-2, 900-2.

Combining the results of XRD, XPS, Raman, TEM, and SAED, it can be seen that graphitic carbon is produced with the catalysis of Ni. In the first step, Ni^{2+} is oxidized to NiO; in the second step, at a specific temperature, NiO reacts with amorphous carbon and is reduced to Ni; in the third step, during the dissolution and precipitation of metallic Ni, it reacts with the surrounding amorphous carbon to form graphitic carbon [19,26].

4. Conclusions

In this paper, we improved the method to achieve low-temperature and highly graphitized pomelo peel to turn waste into a valuable material:

- (1) This paper explores the improved methods and traditional methods for graphitization. With the improved method, the degree of graphitization can reach 80.23% at 900 °C, which is slightly lower than that of commercial graphite (90.23%) and much higher than that of the sample at 900 °C (48.84%) with the traditional method.
- (2) With the improved method, pomelo peels can be transformed into highly graphitized nanospheres at 900 °C. It can be seen from TEM that the plane interlayer spacing of (002) is 0.337 nm, which is very close to the theoretical value of pure graphite (0.3354 nm).
- (3) Whether the traditional method or the improved method is used, the temperature plays an important role in the catalysis of pomelo peel by Ni.
- (4) This work can turn pomelo peels into valuable materials, reduce environmental pollution, and, more importantly, reduce energy consumption and promote sustainable development.

Supplementary Materials: The following supporting information can be downloaded at: <https://www.mdpi.com/article/10.3390/cryst12030403/s1>, Figure S1: XRD pattern of carbonization at 500 °C; Figure S2 (a–c) SEM images of 750-1, 800-1, 900-1; Figure S3 XPS wide scan spectroscopy of the samples; Table S1: Sample synthesis method and renaming; Table S2 Cumulative pore volume and area of micropores for the sample.

Author Contributions: L.Z.: writing—original draft, investigation, formal analysis. Y.W. (Youbin Wang): investigation, validation, writing—review and editing. Y.G.: investigation, validation, writing—review and editing. X.D.: investigation, validation, writing—review and editing. L.C.: investigation, validation, writing—review and editing. N.T.H.N.: investigation, validation, writing—review and editing. C.H.: investigation, validation, writing—review and editing. Y.W. (Yuezhou Wei): investigation, validation, writing—review and editing. G.D.: investigation, validation, writing—review and editing. T.F.: supervision, writing—review and editing. All authors have read and agreed to the published version of the manuscript.

Funding: This work was supported by the National Natural Science Foundation of China (21976039).

Institutional Review Board Statement: Not applicable.

Informed Consent Statement: Not applicable.

Data Availability Statement: Not applicable.

Acknowledgments: The authors would like to thank Shiyanjia Lab (www.shiyanjia.com, accessed date: 17 February 2022) for support of the TEM analysis.

Conflicts of Interest: The authors declare that the research was conducted without any commercial or financial relationships that could be construed as a potential conflict of interest.

References

1. Xiao, L.; Ye, F.; Zhou, Y.; Zhao, G. Utilization of pomelo peels to manufacture value-added products: A review. *Food Chem.* **2021**, *351*, 129247. [[CrossRef](#)] [[PubMed](#)]
2. Chen, X.; Xu, X.; Lu, Z.; Zhang, W.; Yang, J.; Hou, Y.; Wang, X.; Zhou, S.; Li, Y.; Wu, L.; et al. Carbon footprint of a typical pomelo production region in China based on farm survey data. *J. Clean. Prod.* **2020**, *277*, 124041. [[CrossRef](#)]
3. Cheng, D.; Ngo, H.H.; Guo, W.; Chang, S.W.; Nguyen, D.D.; Zhang, X.; Varjani, S.; Liu, Y. Feasibility study on a new pomelo peel derived biochar for tetracycline antibiotics removal in swine wastewater. *Sci. Total Environ.* **2020**, *720*, 137662. [[CrossRef](#)] [[PubMed](#)]
4. Wang, W.; Chen, M. Catalytic degradation of sulfamethoxazole by peroxymonosulfate activation system composed of nitrogen-doped biochar from pomelo peel: Important roles of defects and nitrogen, and detoxification of intermediates. *J. Colloid Interface Sci.* **2022**, *613*, 57–70. [[CrossRef](#)]
5. Wu, M.C.; Zhang, R.H.; Liu, K.; Sun, J.; Chan, K.Y.; Zhao, T.S. Mesoporous carbon derived from pomelo peel as a high-performance electrode material for zinc-bromine flow batteries. *J. Power Sources* **2019**, *442*, 227255. [[CrossRef](#)]

6. Chen, Q.; Tan, X.; Liu, Y.; Liu, S.; Li, M.; Gu, Y.; Zhang, P.; Ye, S.; Yang, Z.; Yang, Y. Biomass-derived porous graphitic carbon materials for energy and environmental applications. *J. Mater. Chem. A* **2020**, *8*, 5773–5811. [[CrossRef](#)]
7. Aval, L.F.; Ghoranneviss, M.; Pour, G.B. High-performance supercapacitors based on the carbon nanotubes, graphene and graphite nanoparticles electrodes. *Heliyon* **2018**, *4*, e00862. [[CrossRef](#)]
8. Ma, Y.; Hu, Z.; Huo, K.; Lu, Y.; Hu, Y.; Liu, Y.; Hu, J.; Chen, Y. A practical route to the production of carbon nanocages. *Carbon* **2005**, *43*, 1667–1672. [[CrossRef](#)]
9. Cassell, A.M.; Raymakers, J.A.; Kong, J.; Dai, H. Large scale CVD synthesis of single-walled carbon nanotubes. *J. Phys. Chem. B* **1999**, *103*, 6484–6492. [[CrossRef](#)]
10. Sevilla, M.; Sanchis, C.; Valdés-Solís, T.; Morallón, E.; Fuertes, A.B. Direct synthesis of graphitic carbon nanostructures from saccharides and their use as electrocatalytic supports. *Carbon* **2008**, *46*, 931–939. [[CrossRef](#)]
11. Fan, C.-L.; He, H.; Zhang, K.-H.; Han, S.-C. Structural developments of artificial graphite scraps in further graphitization and its relationships with discharge capacity. *Electrochim. Acta* **2012**, *75*, 311–315. [[CrossRef](#)]
12. Huang, S.; Guo, H.; Li, X.; Wang, Z.; Gan, L.; Wang, J.; Xiao, W. Carbonization and graphitization of pitch applied for anode materials of high power lithium ion batteries. *J. Solid State Electrochem.* **2013**, *17*, 1401–1408. [[CrossRef](#)]
13. Zhang, S.; Liu, Q.; Zhang, H.; Ma, R.; Li, K.; Wu, Y.; Teppen, B.J. Structural order evaluation and structural evolution of coal derived natural graphite during graphitization. *Carbon* **2020**, *157*, 714–723. [[CrossRef](#)]
14. Liu, H.; Cheng, C.; Wu, H. Sustainable utilization of wetland biomass for activated carbon production: A review on recent advances in modification and activation methods. *Sci. Total Environ.* **2021**, *790*, 148214. [[CrossRef](#)] [[PubMed](#)]
15. Danish, M.; Ahmad, T. A review on utilization of wood biomass as a sustainable precursor for activated carbon production and application. *Renew. Sustain. Energy Rev.* **2018**, *87*, 1–21. [[CrossRef](#)]
16. Li, H.; Zhang, H.; Li, K.; Zhang, J.; Sun, M.; Su, B. Catalytic graphitization of coke carbon by iron: Understanding the evolution of carbon Structure, morphology and lattice fringes. *Fuel* **2020**, *279*, 118531. [[CrossRef](#)]
17. Wang, K.; Cao, Y.; Wang, X.; Kharel, P.R.; Gibbons, W.; Luo, B.; Gu, Z.; Fan, Q.; Metzger, L. Nickel catalytic graphitized porous carbon as electrode material for high performance supercapacitors. *Energy* **2016**, *101*, 9–15. [[CrossRef](#)]
18. Thompson, E.; Danks, A.E.; Bourgeois, L.; Schnepf, Z. Iron-catalyzed graphitization of biomass. *Green Chem.* **2015**, *17*, 551–556. [[CrossRef](#)]
19. Gomez-Martin, A.; Martinez-Fernandez, J.; Rutttert, M.; Heckmann, A.; Winter, M.; Placke, T.; Ramirez-Rico, J. Iron-Catalyzed Graphitic Carbon Materials from Biomass Resources as Anodes for Lithium-Ion Batteries. *ChemSusChem* **2018**, *11*, 2776–2787. [[CrossRef](#)]
20. Sevilla, M.; Fuertes, A.B. Graphitic carbon nanostructures from cellulose. *Chem. Phys. Lett.* **2010**, *490*, 63–68. [[CrossRef](#)]
21. Yan, Q.; Li, J.; Zhang, X.; Hassan, E.B.; Wang, C.; Zhang, J.; Cai, Z. Catalytic graphitization of kraft lignin to graphene-based structures with four different transitional metals. *J. Nanopart. Res.* **2018**, *20*, 223. [[CrossRef](#)]
22. Destyorini, F.; Yudianti, R.; Irmawati, Y.; Hardiansyah, A.; Hsu, Y.-I.; Uyama, H. Temperature driven structural transition in the nickel-based catalytic graphitization of coconut coir. *Diam. Relat. Mater.* **2021**, *117*, 108443. [[CrossRef](#)]
23. Fujimoto, H. Theoretical X-ray scattering intensity of carbons with turbostratic stacking and AB stacking structures. *Carbon* **2003**, *41*, 1585–1592. [[CrossRef](#)]
24. Zou, L.; Huang, B.; Huang, Y.; Huang, Q.; Wang, C.A. An investigation of heterogeneity of the degree of graphitization in carbon-carbon composites. *Mater. Chem. Phys.* **2003**, *82*, 654–662. [[CrossRef](#)]
25. Qiu, T.; Yang, J.-G.; Bai, X.-J.; Wang, Y.-L. The preparation of synthetic graphite materials with hierarchical pores from lignite by one-step impregnation and their characterization as dye absorbents. *RSC Adv.* **2019**, *9*, 12737–12746. [[CrossRef](#)]
26. Sevilla, M.; Sanchis, C.; Valdes-Solis, T.; Morallon, E.; Fuertes, A.B. Synthesis of graphitic carbon nanostructures from sawdust and their application as electrocatalyst supports. *J. Phys. Chem. C* **2007**, *111*, 9749–9756. [[CrossRef](#)]
27. Destyorini, F.; Irmawati, Y.; Hardiansyah, A.; Widodo, H.; Yahya, I.N.D.; Indayaningsih, N.; Yudianti, R.; Hsu, Y.-I.; Uyama, H. Formation of nanostructured graphitic carbon from coconut waste via low-temperature catalytic graphitization. *Eng. Sci. Technol. Int. J.* **2021**, *24*, 514–523.
28. Zha, Z.; Zhang, Z.; Xiang, P.; Zhu, H.; Shi, X.; Chen, S. Porous graphitic carbon from mangosteen peel as efficient electrocatalyst in microbial fuel cells. *Sci. Total Environ.* **2021**, *764*, 142918. [[CrossRef](#)]
29. Hu, C.; Sedghi, S.; Silvestre-Albero, A.; Andersson, G.G.; Sharma, A.; Pendleton, P.; Rodríguez-Reinoso, F.; Kaneko, K.; Biggs, M.J. Raman spectroscopy study of the transformation of the carbonaceous skeleton of a polymer-based nanoporous carbon along the thermal annealing pathway. *Carbon* **2015**, *85*, 147–158. [[CrossRef](#)]
30. Kim, T.; Lee, J.; Lee, K.-H. Full graphitization of amorphous carbon by microwave heating. *RSC Adv.* **2016**, *6*, 24667–24674. [[CrossRef](#)]
31. Liu, X.; Zhou, Y.; Zhou, W.; Li, L.; Huang, S.; Chen, S. Biomass-derived nitrogen self-doped porous carbon as effective metal-free catalysts for oxygen reduction reaction. *Nanoscale* **2015**, *7*, 6136–6142. [[CrossRef](#)] [[PubMed](#)]
32. Schuepfer, D.B.; Badaczewski, F.; Guerra-Castro, J.M.; Hofmann, D.M.; Heiliger, C.; Smarsly, B.; Klar, P.J. Assessing the structural properties of graphitic and non-graphitic carbons by Raman spectroscopy. *Carbon* **2020**, *161*, 359–372. [[CrossRef](#)]
33. Chu, P.K.; Li, L. Characterization of amorphous and nanocrystalline carbon films. *Mater. Chem. Phys.* **2006**, *96*, 253–277. [[CrossRef](#)]
34. Bao, C.; Shi, K.; Xu, P.; Yang, L.; Chen, H.; Dai, Y.; Liu, H. Purification effect of the methods used for the preparation of the ultra-high purity graphite. *Diam. Relat. Mater.* **2021**, *120*, 108704. [[CrossRef](#)]

35. Gong, Y.; Li, D.; Luo, C.; Fu, Q.; Pan, C. Highly porous graphitic biomass carbon as advanced electrode materials for supercapacitors. *Green Chem.* **2017**, *19*, 4132–4140. [[CrossRef](#)]
36. Huang, H.; Guo, T.; Wang, K.; Li, Y.; Zhang, G. Efficient activation of persulfate by a magnetic recyclable rape straw biochar catalyst for the degradation of tetracycline hydrochloride in water. *Sci. Total Environ.* **2021**, *758*, 143957. [[CrossRef](#)]
37. Liou, T.-H.; Wang, S.-Y.; Lin, Y.-T.; Yang, S. Sustainable utilization of rice husk waste for preparation of ordered nanostructured mesoporous silica and mesoporous carbon: Characterization and adsorption performance. *Colloids Surf. A Physicochem. Eng. Asp.* **2022**, *636*, 128150. [[CrossRef](#)]
38. Hou, K.; Yang, X.; Bao, M.; Chen, F.; Tian, H.; Yang, L. Composition, characteristics and antioxidant activities of fruit oils from *Idesia polycarpa* using homogenate-circulating ultrasound-assisted aqueous enzymatic extraction. *Ind. Crops Prod.* **2018**, *117*, 205–215. [[CrossRef](#)]
39. Cao, L.; Zhang, X.; Xu, Y.; Xiang, W.; Wang, R.; Ding, F.; Hong, P.; Gao, B. Straw and wood based biochar for CO₂ capture: Adsorption performance and governing mechanisms. *Sep. Purif. Technol.* **2022**, *287*, 120592. [[CrossRef](#)]
40. Anton, R. On the reaction kinetics of Ni with amorphous carbon. *Carbon* **2008**, *46*, 656–662. [[CrossRef](#)]
41. Zhang, P.; Tan, X.; Liu, S.; Liu, Y.; Zeng, G.; Ye, S.; Yin, Z.; Hu, X.; Liu, N. Catalytic degradation of estrogen by persulfate activated with iron-doped graphitic biochar: Process variables effects and matrix effects. *Chem. Eng. J.* **2019**, *378*, 122141. [[CrossRef](#)]
42. Gai, L.; Li, J.; Wang, Q.; Tian, R.; Li, K. Evolution of biomass to porous graphite carbon by catalytic graphitization. *J. Environ. Chem. Eng.* **2021**, *9*, 106678. [[CrossRef](#)]